# Non-noble metal thickness-tunable $Bi_2MoO_6$ nanosheets for highly efficient visible-light-driven nitrobenzene reduction into aniline

Yanyu Xie, Xiaotong Shang, Dan Liu, Huibo Zhao, Yuyao Gu, Zizhong Zhang*, Xuxu Wang*

*State Key Laboratory of Photocatalysis on Energy and Environment, Research Institute of Photocatalysis, College of Chemistry, Fuzhou University, PR China*

## ARTICLE INFO

## ABSTRACT

High efficiency and selectivity is significant for photocatalytic organic transformation. In this work, the efficient photocatalytic reduction of nitrobenzene into aniline is achieved on non-noble metal thickness-tunable bismuth molybdate nanosheets prepared by the simple hydrothermal reaction. The photocatalytic activity of $Bi_2MoO_6$ strongly depends on the nanosheet thickness. The $Bi_2MoO_6$ monolayer displays remarkably enhanced photocatalytic activity for selective reduction of nitrobenzene than bilayer, multilayers and bulk $Bi_2MoO_6$ due to the unique properties of 2D materials with the large fraction of surface atoms and the ultrafast charge separation. The obtained conversion rate of 487.5 $\mu mol\,g^{-1}\cdot h^{-1}$ (> 95% conversion and > 99% selectivity within 60 min reaction) on $Bi_2MoO_6$ monolayers is 5 times higher than that of $Bi_2MoO_6$ bulk, far exceeding most of common photocatalysts up to date. This work provides a thickness dependent nanosheet concept in the design of newly highly efficient catalysts for the photocatalytic reduction conversion of nitroarenes to anilines.

## 1. Introduction

Photocatalysis has great potential as a renewable and green strategy for organic synthesis in comparison with the conventional synthetic pathways, and thus has attracted considerable attention in recent years [1–3]. Both high efficiency and selectivity of organic transformation is of great significance for photocatalytic application, but still remains a challenging problem due to the serious recombination of photoinduced electron/hole pairs and the strong redox ability of electrons and holes. Many efforts have been devoted to engineering photocatalysts and re-action systems for promoting the conversion of organic reactants into target products [4–6].

The reduction conversion of nitroarenes to their substituted anilines is very important in organic synthesis and applied on large scale for a variety of fine chemicals, pesticides and pharmaceuticals [7–9]. Many traditional heterogeneous catalysts have been developed for the hy-drogenation of nitrobenzene to anilines, such as $Au/TiO_2$ [10], Pd/C [11], $Pd/Al_2O_3$ [12], $Pd/TiO_2$ [13], $PtZn/SiO_2$ [14], and MoPt/C [15]. Unfortunately, these catalytic systems require high temperature, high $H_2$ gas pressure and noble metal catalysts. Especially, noble metals such as Pd or Pt have limitation of low selectivity [16,17], while Au nano-particles have poor activity [18–22]. Up to date, it is still a challenge for the efficient selective reduction of nitroaromatic compounds under mild conditions.

Photocatalytic reduction from nitroarenes to anilines has been achieved on the solar-driven nanostructure semiconductor materials. Most studies are based on the plasmonic metal supported photocatalysts for the effective photoreduction of nitroaromatic compounds producing aniline compounds, such as Pt [23,24], Au [25] or Ag/Au [26] coca-talysts combining with $TiO_2$, $Au/KNbO_3$ [27], Au-loaded $Na_2Ta_2O_6$ [28]. For example, $WO_3$-Ag hybrid nanowires has been reported for nitro reduction reactions in methanol solvent under visible light irra-diation with an obtained conversion rate of 81.2 $\mu mol\,h^{-1}\,g^{-1}$ [29]. Aniline can be successfully synthesized at room temperature by using Ag supported $Bi_2MoO_6$ photocatalyst for 120 min irradiation and the concentration of nitrobenzene is $8.13 \times 10^{-4}$ $mol\cdot L^{-1}$ [30]. Although heterogeneous metal-loaded photocatalysts show reasonable perfor-mance in nitrobenzene reduction, the cost of the material and the low photocatalytic efficiencies render their large-scale application diffi-culty. Moreover, compared to their semiconductor counterpart, the supported plasmonic metal nanoparticle based photocatalysts show relatively low efficiency for light absorption. To overcome the low light absorption and the high economic costs of noble metal, some non-precious metal cocatalysts or visible-light active semiconductor pho-tocatalysts have been developed. For example, the reduced graphene oxide (NS-rGO) modified CdS photocatalysts can selectively converts nitrobenzene to aniline under visible light irradiation [31]. However, using graphene support need an interface contact and appropriate

---

matching between the band positions, which limits its commercial potential. CoP decorated CdS nanowires has been reported for nitrobenzene reduction into azobenzene and aniline [32], as comparable to that of the catalysts formed using a noble metal loaded onto CdS. Nevertheless, CdS is the unstable for the photoreaction and toxic for green chemistry. Therefore, the development of a visible light active photocatalyst for the highly efficient and selective reduction of nitrobenzene to aminobenzene is still as a knotty difficulty.

As one typical members of the Aurivillius family, bismuth molybdate ($Bi_2MoO_6$) consisting of perovskite-like layers of $[MoO_4]^{2-}$ sandwiched between bismuth oxide $[Bi_2O_2]^{2+}$ layers has shown impressive photocatalytic performance in organic contaminant decomposition [33], photoelectrochemical water splitting [34], photoreduction of carbon dioxide [35], organic transformations [36], due to the relatively narrow bandgap of ~2.7 eV to solar light utilization and its suitable energy band positions. However, the photocatalytic performance of $Bi_2MoO_6$ is still far from satisfactory because of the high recombination rate of photogenerated electron–hole pairs [37]. Recently, monolayer and several atomic layer two-dimensional (2D) materials have attracted massive attention for the prominent merits such as more active sites with larger specific surface area and prolonged photocarrier lifetime because of spatial confinement effects [38–42]. Benefiting from the atomic thickness and high ratio of surface atoms to entire atoms, the ultrathin 2D materials exhibit unique physicochemical properties, such as tunable energy band structure and high surface activity [43–45]. Taking into account the unique properties of 2D materials, there is an optimistic expectation toward the photocatalytic performance of $Bi_2MoO_6$ in the reduction of nitrobenzene to aniline.

Herein, we fabricated non-noble metal ultrathin $Bi_2MoO_6$ nanosheets by a simple hydrothermal route for the photocatalytic nitrobenzene reduction into aniline with a high efficiency and selectivity. The lateral size from monolayer to multilayer of obtained ultrathin $Bi_2MoO_6$ nanosheets can be tuned by changing synthesis temperature. $Bi_2MoO_6$ monolayer samples exhibited the highest photocatalytic activity among the photocatalysts of $Bi_2MoO_6$ bilayer, multilayer and bulk. The obtained conversion rate of $487.5 \, \mu mol \, g^{-1} \cdot h^{-1}$ (> 95% conversion and > 99% selectivity within 60 min reaction) is 5 times higher than that of $Bi_2MoO_6$ bulk, far exceeding most of common photocatalysts up to date. This is because the $Bi_2MoO_6$ monolayers are dominant advantageous for enhancing the light absorption and separating of photogenerated electron–hole pairs. This study is able to explore further into other similar selective reduction of nitro compounds for a better photocatalytic application.

## 2. Experimental

### 2.1. Catalyst preparation

The ultrathin $Bi_2MoO_6$ nanosheets were prepared by a simple hydrothermal reaction. In detail, 1 mmol $Na_2MoO_4 \cdot 2H_2O$, 2 mmol $Bi(NO_3)_3 \cdot 5H_2O$ and 0.05 g hexadecyl trimethyl ammonium Bromide (CTAB) were added to 80 ml deionized water for 30 min stirring. The mixed solution was transferred into a 100 ml Teflon-lined autoclave and was sealed into a stainless steel tank for hydrothermal reaction. The hydrothermal temperature was controlled at 160 °C, 140 °C, 120 °C, 100 °C and 90 °C for 24 h, respectively. Finally, the product was collected and washed several times with deionized water and dried at 60 °C in air for 8 h. The obtained samples were marked as BMO-160, BMO-140, BMO-120, BMO-100 and BMO-90 according to the hydrothermal temperature. The bulk $Bi_2MoO_6$ was prepared without CTAB assistances in the similar hydrothermal processes.

### 2.2. Structural characterizations

The X-ray diffraction patterns of the photocatalysts were recorded on a Bruker D8 Advance X-ray diffractometer with Ni filtered Cu Kα

radiation at 40 kV and 40 mA. Ultraviolet–visible diffuse reflectance spectra (DRS) were obtained with a self-supporting sample disk on an ultraviolet–visible spectrophotometer (Cary 500), where $BaSO_4$ was used as a reflectance standard sample. Transmission Electron Microscope (TEM) images were obtained using a JEOL model JEM 2010 EX instrument at an accelerating voltage of 200 kV. Atomic force microscopy (AFM) was collected on a Bruker Dimension Icon. During an AFM experiment, sample was dispersed in ethanol using an ultrasonic bath for 30 min and then the dispersion was diluted in ethanol. A drop of the above diluted dispersion was deposited on a new cleaved mica surface and dried in air. The instrument parameters (set point, amplitude, scan size, scan speed and feedback control) were adjusted for the best resolution of images.

### 2.3. Photocatalytic selective reduction of nitrobenzene

All the photocatalytic reactions were conducted in a 30 ml Pyrex glass reactor and with a magnetic stirrer (600 rmp/min). The specific procedure was as follow: 30 mg photocatalyst sample was dispersed into 10 ml of mixture of nitrobenzene-methanol, which the initial concentration of nitrobenzene is 975 μmol/L. To remove dissolved oxygen from the reaction medium, $N_2$ gas was passed through the reaction medium for 30 min in dark. Then the whole system was sealed up and irradiated with a 300 W Xe lamp with a UV-cut filter to cut off the light of wavelength ≥ 420 nm. During the reaction time, the suspension was filtered through a 0.22 mm nylon syringe filter and then diluted with acetonitrile. The concentrations of nitrobenzene, aniline and other byproducts in the solution were analyzed by using high performance liquid chromatography (HPLC). The conversion of nitrobenzene and yield, selectivity for aniline were as follows:

$$Conversion(\%) = [(C_0 - C_{nitrobenzene})/C_0] \times 100,$$

$$Yield(\%) = [C_{aniline}/C_0] \times 100,$$

$$Selectivity(\%) = [C_{aniline}/(C_0 - C_{nitrobenzene})] \times 100.$$

Where $C_0$ represents the initial concentration of nitrobenzene before illumination, $C_{nitrobenzene}$ and $C_{aniline}$ are the concentrations of the substrate nitrobenzene and the corresponding aniline in solution during the photocatalytic reaction, respectively.

## 3. Results and discussion

### 3.1. Composition and structure

The crystal structure of the prepared BMO nanosheets was characterized by XRD patterns, as shown in Fig. 1a. All the diffraction peak positions were well indexed to an orthorhombic phase BMO (JCPDS No. 21-0102) without any other impurity peaks. The intensity of diffraction peak of BMO nanosheets was dependent on the hydrothermal temperature. When the hydrothermal temperature was started at 80 °C, the diffraction peaks were weak and broad, indicating the amorphous structure of BMO. Increasing the temperature to 90 °C and 100 °C, the diffraction peaks were greatly increased to improve the crystallinity of BMO. Further increasing the temperature (120 °C, 140 °C and 160 °C) led to a gradual increase in the crystallinity. This indicates the growth of the layer thickness of BMO nanosheets at higher temperature. Compared to the bulk BMO sample, the weakened (020) and (131) peaks emerged, clearly showing ultrathin thickness and small particle size of the BMO nanosheets. In order to further clarify the difference among the various ultrathin nanosheets, the magnified XRD diffraction peaks in the range of 30~35° are presented in Fig. 1b. The relative intensities between (060) and (200)/(002) diffraction peak of the BMO-80, BMO-90, BMO-100, BMO-120, BMO-140, BMO-160 samples were increasing, suggesting that the BMO nanosheets preferentially grow along the [010] direction with increasing hydrothermal temperature
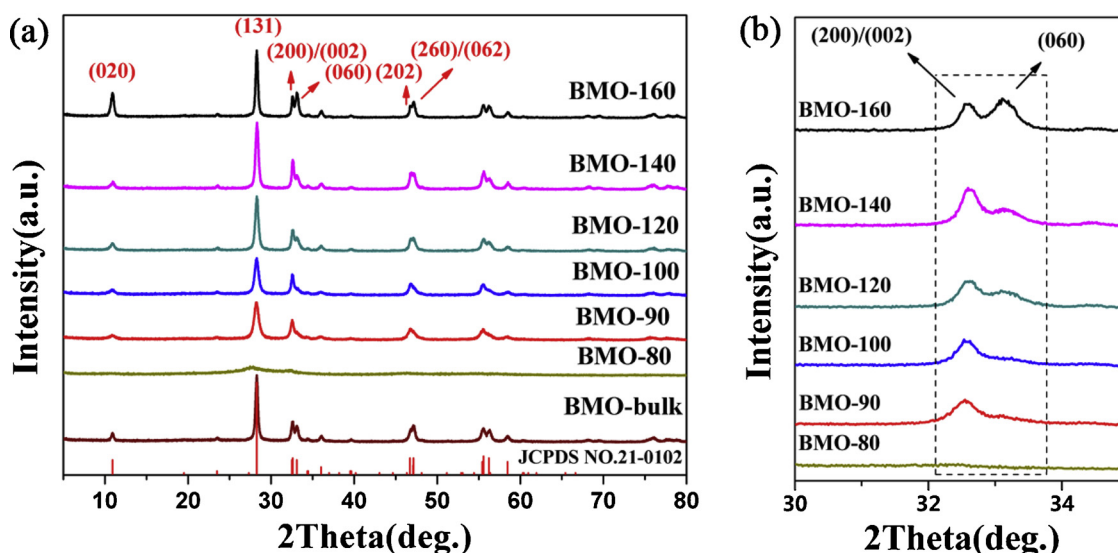
**Fig. 1.** (a) The XRD pattern and (b) Local magnification of XRD patterns of BMO-80, BMO-90, BMO-100, BMO-120, BMO-140, BMO-160 sample.

[33,36].

The TEM and AFM images (Fig. 2) confirmed sheet-shaped structures of the prepared BMO sample dependent on the hydrothermal temperature. BMO-90 sample showed a few amount of the transparent and rigid square-like nanosheets but was surrounded with large amounts of fragments (Fig. 2a), and the selected area electron diffraction (SAED) patterns presented clearly polycrystalline diffraction rings (inset of Fig. 2a), indicating that the BMO was not fully grown into the crystal nanosheets but contained some amorphous structure. The formed BMO-90 nanosheets had a thickness of 0.6 nm estimated from AFM image and the corresponding height histograms (Fig. 2b and c). BMO-100 sample displayed an almost perfect nanosheet structure without small fragments, while the nearly transparent features indicate the ultrathin thickness (Fig. 2d). The high-resolution TEM (HRTEM) image (Fig. S1) demonstrated that the BMO nanosheets grew along the [010] direction. The lattice fringes about 0.275 and 0.274 nm were respectively corresponded to (002) and (200) planes of orthorhombic $Bi_2MoO_6$. This implies that the as-prepared BMO nanosheets preferentially expose the (010) facets. The corresponding selected area electron diffraction (SAED) pattern (inset of Fig. 2d) showed the clear ordered diffraction spots, indicating a single crystal of nanosheets and that all the diffraction planes are perpendicular to the (010) facet. $Bi_2MoO_6$ is a layered material consisting of $[MoO_4]^{2-}$ and $[Bi_2O_2]^{2+}$ with an interlayer distance of 0.81 nm as shown in Fig. 2q. The corresponding AFM height profiles indicate that the BMO-100 nanosheets are of an average thickness of 0.85 nm (Fig. 2e and f), corresponding to monolayer $Bi_2MoO_6$ slab. Increasing the hydrothermal temperature to 120 °C and 140 °C, the nanosheets of BMO-120 and BMO-140 started to be semitransparent (Fig. 2g and i), indicating the growth of thickness of nanosheet. The corresponding AFM height profiles indicate that the BMO-120 and BMO-140 nanosheets are of an average thickness of 1.6 nm (Fig. 2h, i, k and l), corresponding to the size of $Bi_2MoO_6$ unit cell. Apparently, the monolayer $Bi_2MoO_6$ grew up vertically with increasing hydrothermal temperature. As shown in Fig. 2m, the nanosheets of BMO-160 continued to grow vertically and had a thickness of about 4.8 nm, which corresponds to three $Bi_2MoO_6$ unit cell. This strongly demonstrates that the reaction temperature could help to tune the number of layers of bismuth molybdate. As compared, without CTAB assistances in preparation processes, the bulk $Bi_2MoO_6$ showed the random grain morphology. Therefore, with CTAB assistance at 100 °C hydrothermal reaction, the BMO-100 sample displayed a monolayer nanosheet structure with a high crystallinity and a thickness of 0.85 nm. The ultrathin thickness can readily shorten the diffusion length of charge carriers, and the superb crystal quality of BMO nanosheets also excludes the possibility of any grain boundaries and/or other interfaces (which usually act as recombination sites in polycrystalline materials). These features of BMO nanosheets should favor the separation of photogenerated electron/hole pairs and thus contribute to an improved photocatalytic performance. Specific surface areas of BMO nanosheet photocatalysts were measured by the $N_2$ sorption isothermal analysis. The BET surface area (Fig. S2) was gradually decreased from 31.2, 29.1, 22.9, 15.9 to 11.2 $m^2 \cdot g^{-1}$ for BMO-90, BMO-100, BMO-120, BMO-140 and BMO-160 with increasing hydrothermal reaction temperature, which is consistent with the XRD and TEM results. The Raman spectra (Fig. S3) for the BMO nanosheets and bulk with the well defined phonon modes in the 200-900 $cm^{-1}$ wavenumber range, corresponding to the vibrational modes of orthorhombic $Bi_2MoO_6$, confirmed the formation of highly pure $Bi_2MoO_6$.

### 3.2. Photoelectric properties

The light absorption of $Bi_2MoO_6$ nanosheets and bulk $Bi_2MoO_6$ were exhibited by UV–vis diffuse reflectance spectra (DRS), as shown in Fig. 3a. The $Bi_2MoO_6$ nanosheets had a comparative light absorption with BMO bulk for a sharp absorption edge of about 480 nm corresponding the band gap (Eg) of 2.6 eV, which is attributed to the intrinsic absorption band of $Bi_2MoO_6$. This confirmed that the $Bi_2MoO_6$ nanosheets could be a good visible-light-driven photocatalyst for harvesting solar energy. The photocurrent density results of bulk $Bi_2MoO_6$ and a series of $Bi_2MoO_6$ nanosheet electrodes under visible light irradiation were shown in Fig. 3b. It can be seen that the photocurrent densities of the samples are in the order: BMO-100 > BMO-120 > BMO-160 > BMO-90 > BMO-bulk. Obviously, BMO-100 had a maximum photocurrent density among all the $Bi_2MoO_6$ nanosheets, indicating the highest separation efficiency and migration rate for photogenerated carriers, due to the high crystallinity and monolayer thickness of BMO-100. To confirm the enhancing charge transfer for the as-synthesized photocatalysts, the photoluminescence spectra and nyquist impedance plots of the $Bi_2MoO_6$ bulk and various $Bi_2MoO_6$ nanosheets were detected, as shown in Fig. 3c and d. It can be seen that the BMO-100 displayed the lowest photoluminescence intensity and the lowest AC impedance value among various $Bi_2MoO_6$ nanosheets, indicating the best electron transfer rate and separation efficiency on BMO-100 and thus the best photocatalytic performance.
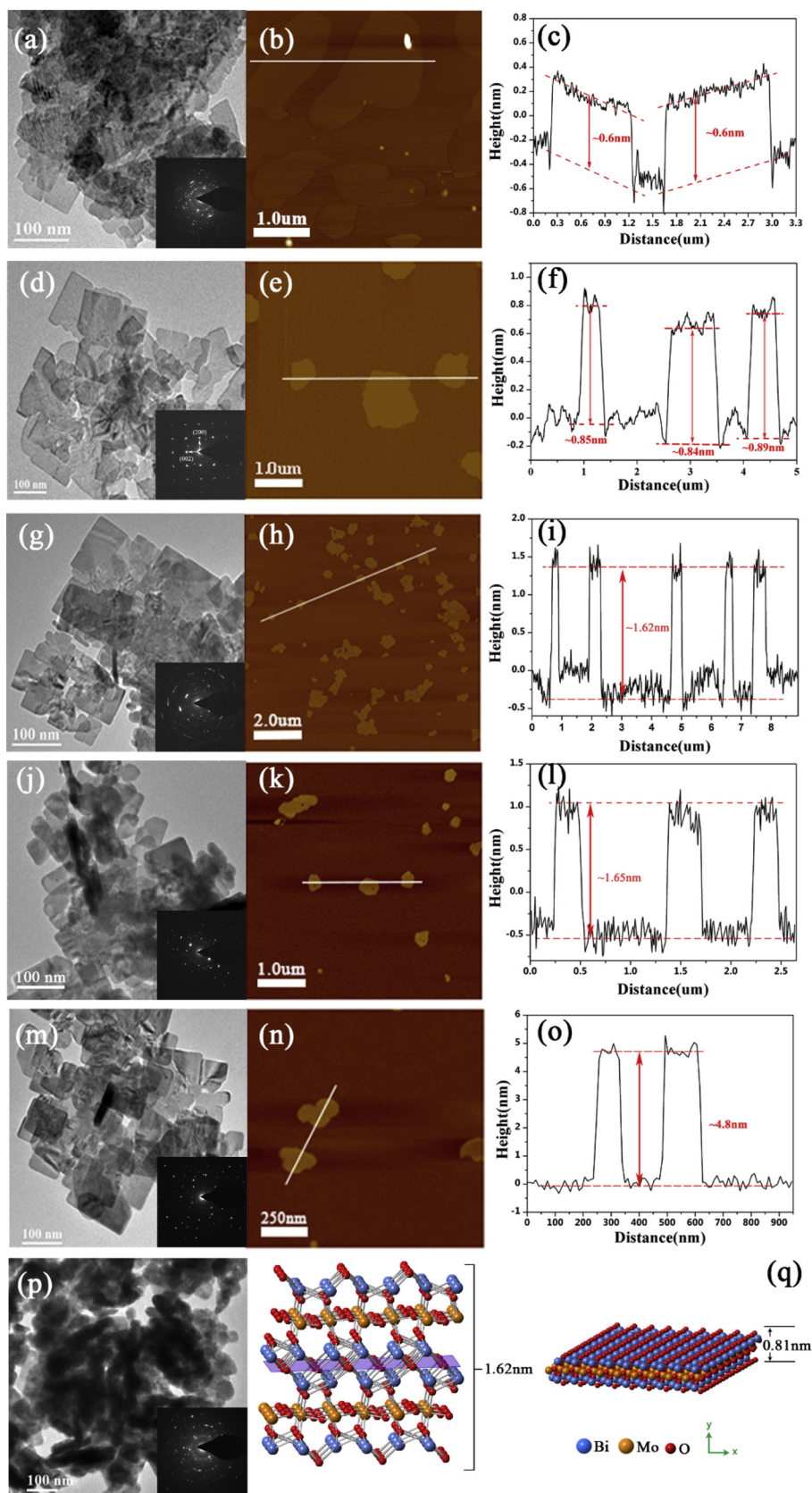
**Fig. 2.** TEM, AFM images and the height profiles of lines of BMO nanosheets, corresponding to samples (a, b, c) BMO-90, (d, e, f) BMO-100, (g, h, i) BMO-120, (j, k, l) BMO-140 and (m, n, o) BMO-160. TEM images of (p) BMO-bulk. (q) Schematic diagram of orthorhombic $Bi_2MoO_6$ crystal structure.
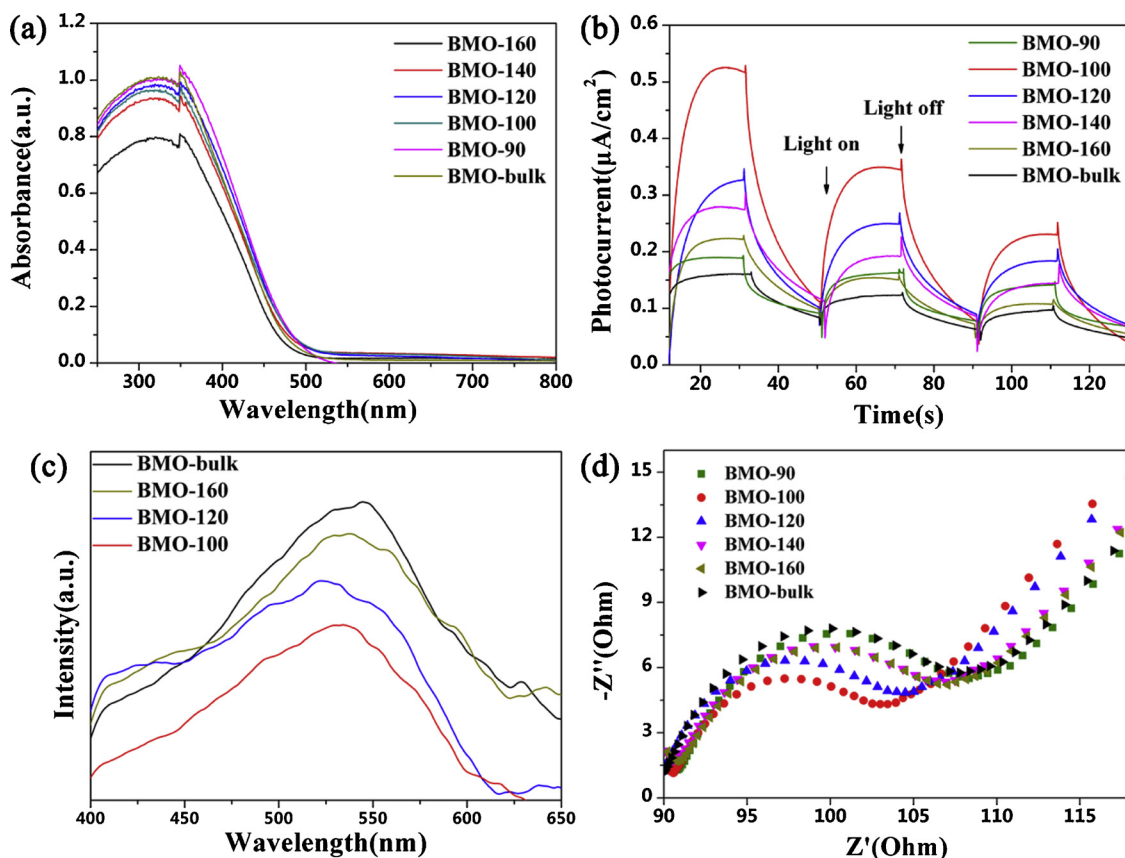
**Fig. 3.** (a) UV–vis diffuse reflectance spectra of BMO-160, BMO-140, BMO-120, BMO-100, BMO-90 and BMO-bulk; (b) transient photocurrent responses under visible light irradiation ($\lambda \geq 420$ nm), (c) Photoluminescence(PL) spectra of the as-synthesized samples. (d) Nyquist impedance plots of the samples.

### 3.3. Photocatalytic activity

The photocatalytic selective reduction of nitrobenzene to aniline was evaluated over various $Bi_2MoO_6$ nanosheets and bulk $Bi_2MoO_6$ under visible light irradiation ($\lambda \geq 420$ nm), as shown in Fig. 4. The conversion of nitrobenzene into aniline was increased with increasing irradiation time over $Bi_2MoO_6$ photocatalysts. For the bulk $Bi_2MoO_6$, only 18.3% of nitrobenzene was conversed within 40 min. As comparison, the conversion of nitrobenzene was significantly enhanced on $Bi_2MoO_6$ nanosheets but depended on the thickness of $Bi_2MoO_6$ nanosheets. Monolayer BMO-100 can completely achieve the conversion of nitrobenzene into aniline within 40 min. When the thickness of $Bi_2MoO_6$ nanosheets was increased by tuning the hydrothermal

reaction temperature, the conversion rate of nitrobenzene was gradually decreased. This indicates that the reduced thickness provides the more effective separation of the photoinduced electron–hole pairs and thus increases the photocatalytic activity. The BMO-100 monolayers exhibited a highest conversion efficiency with a reaction rate of 487.5 $\mu$mol g$^{-1}$·h$^{-1}$, > 93% conversion of the nitrobenzene within 40 min reaction and the selectivity to aniline exceeding > 97.7%. Although the thickness of BMO-90 is thinnest among various $Bi_2MoO_6$ nanosheets, the BMO-90 sample was not fully grown into the crystal nanosheets with some amorphous structure fragments, as seen in TEM images (Fig. 2a). The large difference in the nitrobenzene conversion rates between BMO-90 and BMO-100 can be attributed to the amorphous structure of BMO-90. The surface and interfaces of the low
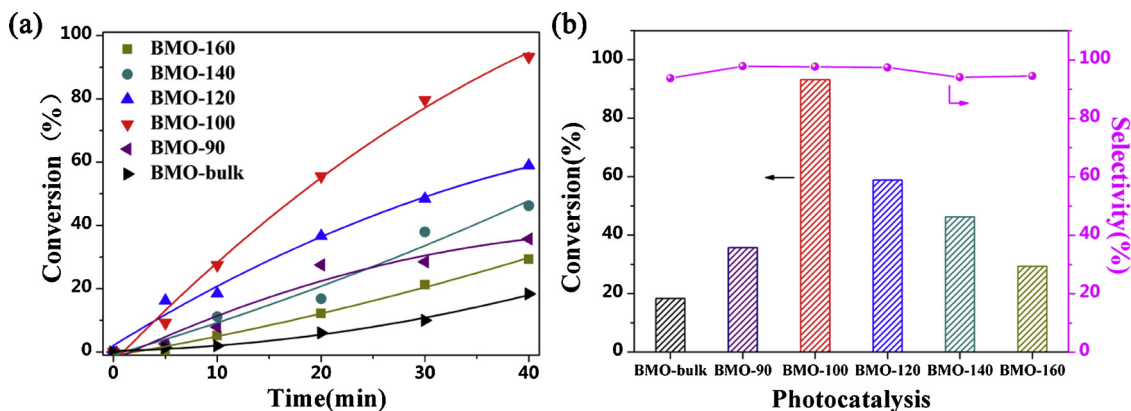


**Fig. 4.** (a) Photoreduction curves of the NB solutions containing different photocatalysts under visible light irradiation ($\lambda \geq 420$ nm); (b) Conversion, selectivity of photocatalytic reduction.
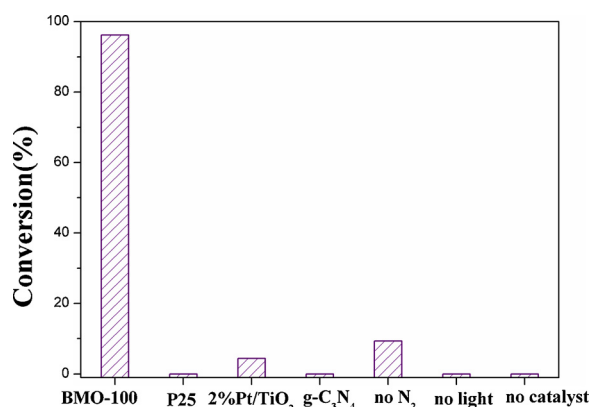
**Fig. 5.** Photocatalytic conversion of nitrobenzene for the control experiment.

crystallinity of $Bi_2MoO_6$ usually act as recombination sites for the photogenerated electron/hole pairs to result in the low photocatalytic nitrobenzene conversion [46–48].

Moreover, the typical photocatalysts including Degussa P25 $TiO_2$, $Pt/TiO_2$ and graphitic carbon nitride g-$C_3N_4$ were also used to evaluate the photocatalytic conversion of nitrobenzene (Fig. 5). However, $TiO_2$, 2 wt%$Pt/TiO_2$ and g-$C_3N_4$ had a very low conversion rate (< 4.4%) of nitrobenzene for 60 min reaction under similar conditions. The controlling experimental with either no light irradiation or no catalyst verified that no conversion of nitrobenzene occurred. Moreover, we also prepared the microsphere $Bi_2MoO_6$ samples [49] and used them for photocatalytic nitrobenzene reduction for comparison with bulk and monolayer $Bi_2MoO_6$, as shown in Fig. S5. It clearly shows that monolayer BMO-100 samples have a much better activity than microsphere $Bi_2MoO_6$ samples does. For comparison of nitrobenzene conversion rates with different ultra-thin nanosheet photocatalysts, we synthesized monolayer $Bi_2WO_6$ [50], the BiOBr [51] and BiOCl [52] nanosheets according to the literatures. However, monolayer $Bi_2WO_6$, BiOBr and BiOCl nanosheets had a very low conversion efficiency of nitrobenzene under similar conditions, as shown in Fig. S6. All these results clearly show the advantage of monolayer $Bi_2MoO_6$ nanosheets for the selective photocatalytic reduction of nitrobenzene to aniline.

To prove the general universality of monolayer $Bi_2MoO_6$ nanosheet for the reduction reaction, the reduction of other nitroarenes was evaluated under visible light irradiation. The effect of different substituents containing electron-donating and electron-withdrawing groups and their position on the conversion efficiency of nitrobenzene was studied (Table 1). The various nitroarenes were well reduced on $Bi_2MoO_6$ nanosheets toward their corresponding anilines in excellent

yield and selectivity irrespective of substituent groups under visible light irradiation at room temperature. Some substituent groups on benzene ring was susceptible to reduction during nitro reduction, nevertheless, these substituents were kept unchange and anilines were observed with high selectivity on the $Bi_2MoO_6$ nanosheets. This demonstrates again the excellent photocatalytic activity of the monolayer $Bi_2MoO_6$ nanosheets for the selective reduction of nitroarenes. On the whole, electron-withdrawing groups to the nitrobenzene, such as −Cl and N−$O_2$ groups, displayed a much higher conversion of nitroarenes. On the contrary, electron donor groups decrease the conversion of nitroarenes, such as −$OCH_3$ and N−$H_2$. This is very reasonable because the placement of an electron-withdrawing substituent can decrease the electron density of the −$NO_2$ group, thus activating the nitroarane toward reduction. When an electron-donating group is present in the aromatic ring, the ability of the nitro group to accept electrons is weakened and cannot be easily reduced. With respect to the position of the substituents, the para substituents had a higher reactivity than the meta substituents in the reduction of nitroarenes into their corresponding anilines for either electron-donating or electron-withdrawing groups, such as −$NH_2$ and N−$O_2$.

The recycle durability of BMO-100 monolayers was investigated (Fig. 6). BMO-100 monolayers were successfully reused for more than five cycles without any obvious loss of catalytic activity for the complete conversion of nitrobenzene. This indicates the high activity and stability of monolayer $Bi_2MoO_6$ nanosheet for the selective photocatalytic reduction of nitrobenzene to aniline.

### 3.4. Mechanism of the nitrobenzene reduction on $Bi_2MoO_6$ nanosheets

It has been reported that there are two main pathways for the reduction of nitrobenzene to aniline by the photocatalytic processes in Scheme 1. One is involved the stepwise reduction through nitroso and hydroxylamine intermediates to aniline (pathway A). The other is involved the coupling intermediates such as azobenzene and azoxybenzene to aniline (pathway B). To understand the mechanistic route of the reduction of nitrobenzene on $Bi_2MoO_6$ nanosheets, we used the important intermediates nitroso or azobenzene as the starting reactants for the photocatalytic reduction over $Bi_2MoO_6$ under the similar reaction conditions. As summarized in Table 2, when azobenzene was employed as the starting reactants, no aniline products was yielded in the $Bi_2MoO_6$ system under visible light irradiation for 60 min reaction. However, in the case of nitroso as the starting reactants, nitroso can be completely conversed into aniline with a short time of 30 min over $Bi_2MoO_6$ nanosheet photocatalyst. Obviously, the photocatalytic reduction mechanism of nitrobenzene to aniline over $Bi_2MoO_6$ nanosheets should follow the pathway A. Nitrobenzene was transformed into aniline by the stepwise reduction of nitrobenzene through nitroso and hydroxylamine intermediates.

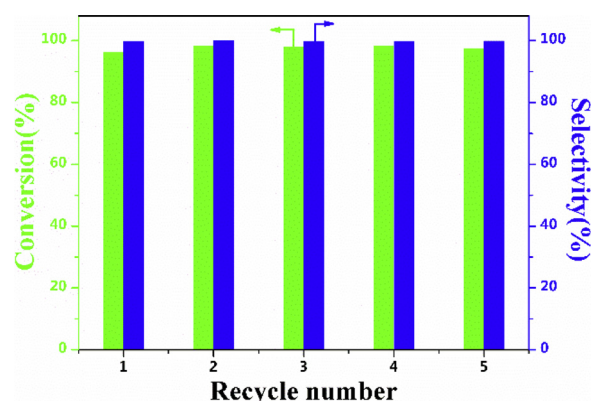In generally, the each step from nitrobenzene to nitroso to

**Table 1**
Photocatalytic reduction of substituted nitroaromatics using the BMO-100.

| Substrates | Products | t(h) | Conv.(%) | Sel.(%) |
|---|---|---|---|---|
| ⬡−$NO_2$ | ⬡−$NH_2$ | 1 | 96.5 | 100 |
| Cl−⬡−$NO_2$ | Cl−⬡−$NH_2$ | 1 | 88.3 | 92.3 |
| $H_3CO$−⬡−$NO_2$ | $H_3CO$−⬡−$NH_2$ | 1 | 68 | > 99 |
| $H_2N$−⬡−$NO_2$ | $H_2N$−⬡−$NH_2$ | 1 | 64.5 | 93.7 |
| $H_2N$−⬡−$NO_2$ | $H_2N$−⬡−$NH_2$ | 1 | 47.5 | 87.7 |
| $O_2N$−⬡−$NO_2$ | $H_2N$−⬡−$NO_2$ | 1 | 100 | 56.5 |
|  | $H_2N$−⬡−$NH_2$ | 2 | 100 | > 99 |
| $O_2N$−⬡−$NO_2$ | $H_2N$−⬡−$NO_2$ | 1 | 83.3 | 33.6 |
|  | $H_2N$−⬡−$NH_2$ | 2 | 100 | 86.6 |



**Fig. 6.** NB conversion of BMO-100 in a series of consecutive catalytic tests.
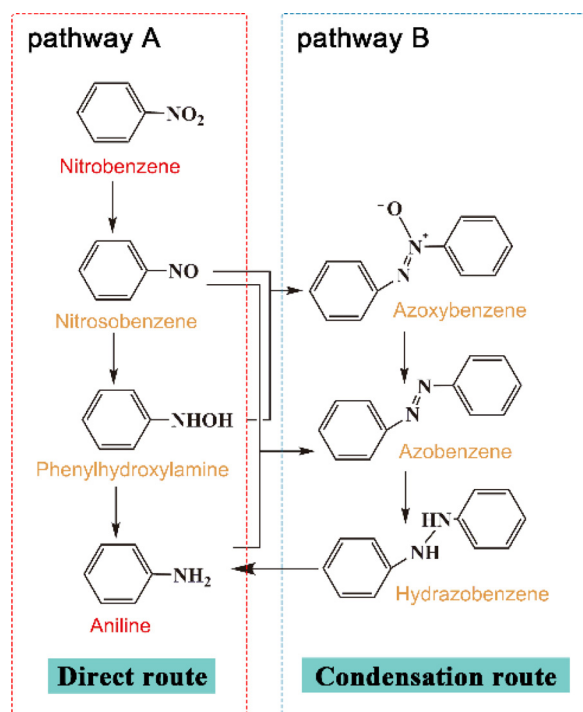
**Scheme 1.** Reaction mechanism of the reduction of nitrobenzene reduction to anilines proposed by Haber.

**Table 2**
Photocatalytic activity of BMO-100 with different substrates for reaction pathway study.

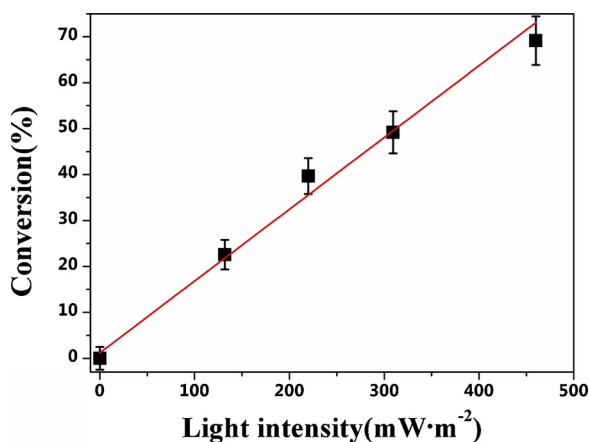| Entry | Substrates | t(h) | Conv.(%) | Sel.(%) |
|---|---|---|---|---|
| 1 | Nitrobenzene | 1 | 96.2 | 99.8 |
| 2 | Nitrosobenzene | 0.5 | 98 | 99.4 |
| 3 | Azobenzene | 2 | 26.8 | 0 |
| 4 | Azoxybenzene | 2 | 21.7 | 0 |



**Fig. 7.** Dependence of nitrobenzene conversion on the intensity of light irradiation over BMO-100.

hydroxylamine to final aniline involves two photogenerated electrons and two protons. To understand which step is rate-limiting for the overall reaction of nitrobenzene reduction to aniline, we determined the dependence of nitrobenzene conversion on the light intensity of visible light irradiation (420 ˜ 800 nm). We observed that the nitrobenzene conversion is linearly increased with increasing light intensity in the range of 0 ˜ 450 mW/cm$^2$, as shown in Fig. 7. This also

indicates the nitrobenzene reduction into aniline driven by the light-excited electrons. More importantly, such a linear dependence suggests that this is a single-photon (or single-electron) rather than a multi-photon driven chemical process. The photocatalytic reaction over $Bi_2MoO_6$ nanosheets has a rate-determining step that is one electron-driven chemical process at the microscopic mechanism. In the all elementary reaction steps, the one-electron transfer to nitrobenzene to form the adsorbed one-electron intermediates is the rate-determining step of overall reaction due to the massive energy cost of reorganizing of the stable nitro group to form the radical anion. All subsequent electron- and proton-transfer steps to finally form aniline are energetically downhill and easy [53,54]. Based on the above results, a tentative mechanism for the photocatalytic nitrobenzene conversion into aniline over $Bi_2MoO_6$ nanosheets was proposed in Fig. 8. It has been reported that valence band of $Bi_2MoO_6$ primarily consists of O 2p orbitals and its conduction band is composed of dominatingly the Mo 4d orbitals in $MoO_4$ octahedra [55]. Because $Bi_2MoO_6$ nanosheets consist of perovskite-like layers of $[MoO_4]^{2-}$ sandwiched between bismuth oxide $[Bi_2O_2]^{2+}$ layers. Under visible light irradiation, the excited electron on $Bi_2MoO_6$ monolayers was migrated to the nanosheet edge to activate the $-NO_2$ group, following by the further electron- and proton-transfer steps to produce nitrosobenzene and phenyhydroxylamine intermediates, and finally to aniline. With increasing the light intensity, the number of excited electrons was increased, which result in the transfer of more electrons to nitrobenzene molecules and thus enhance the photocatalytic aniline yield. Holes on $Bi_2MoO_6$ nanosheets were consumed by the oxidation of methanol into formaldehyde. To confirm the mechanism of nitrobenzene conversion on $Bi_2MoO_6$ monolayers, the quenching experiments were conducted to choose $CCl_4$ as a scavenger for trapping photogenerated electrons and replace the methanol solvent with acetonitrile to reduce the consumption of the photogenerated holes (Fig. S7), respectively. When 5 μL $CCl_4$ was added into the reaction system, the conversion of nitrobenzene was obviously decreased, implying that the photogenerated electrons are the major reductive species for the selective reduction of nitrobenzene. On the other hand, when the solvent is changed to acetonitrile, the conversion of nitrobenzene decreased obviously. It is clear that the methanol also is necessary for the highly efficient conversion of nitrobenzene. In order to make sure the role of methanol in the reaction as an electron donor or just hydrogen source for nitrobenzene hydrogenation, we used BMO-100 samples for photocatalytic nitrobenzene reduction in an acetonitrile solution with hydrogen atmosphere. Only a slight of nitrobenzene is reduced into aniline under hydrogen atmosphere (Fig. S8). Obviously, for the high efficient nitrobenzene conversion, methanol is mainly played as a scavenger for trapping photogenerated holes to enhance the nitrobenzene reduction from the photogenerated electrons on $Bi_2MoO_6$.

## 4. Conclusions

This study has demonstrated that $Bi_2MoO_6$ monolayers are an excellent photocatalyst for the selective reduction of nitro compounds to the corresponding anilines as the sole products driven by visible-light irradiation. The photocatalytic nitrobenzene reduction over $Bi_2MoO_6$ nanosheets has a rate-determining step that is one electron-driven chemical process at the microscopic mechanism. The highly efficient nitrobenzene conversion over $Bi_2MoO_6$ nanosheets can be attributed to (1) the ultrathin thickness can readily shorten the diffusion length of charge carriers, (2) the superb crystal quality of $Bi_2MoO_6$ nanosheets also excludes the possibility of any grain boundaries and/or other interfaces (which usually act as recombination sites in polycrystalline materials).

### Declaration of competing interest

The authors declare that they have no known competing financial
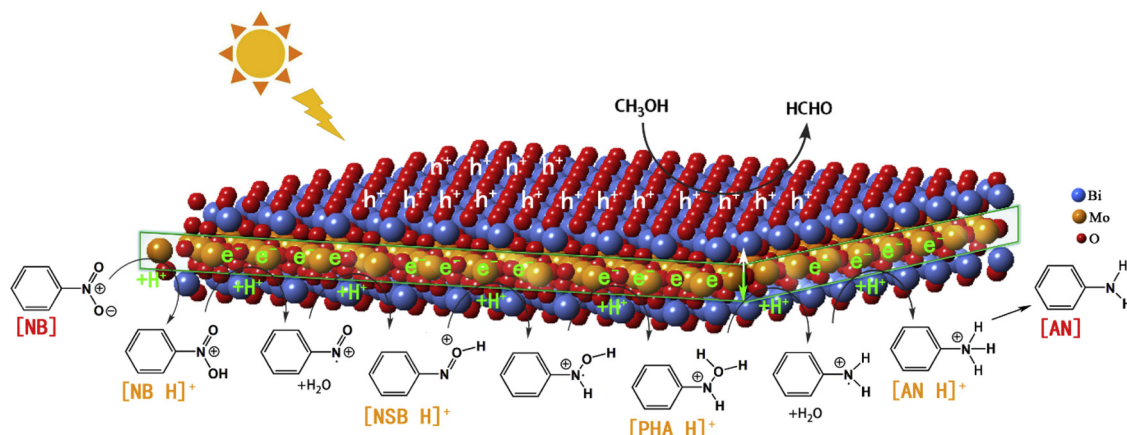
**Fig. 8.** The proposed mechanism of the photocatalytic nitrobenzene conversion into aniline on $Bi_2MoO_6$ nanosheets.

interests or personal relationships that could have appeared to influence the work reported in this paper.

## Acknowledgements

## Appendix A. Supplementary data

Supplementary material related to this article can be found, in the online version, at doi:https://doi.org/10.1016/j.apcatb.2019.118087.

## References

[1] J. Kou, C. Lu, J. Wang, Y. Chen, Z. Xu, R.S. Varma, Selectivity enhancement in heterogeneous photocatalytic transformations, Chem. Rev. 117 (2017) 1445–1514.

[2] J.W. Tucker, J.M.R. Narayanam, S.W. Krabbe, C.R.J. Stephenson, Electron transfer photoredox catalysis: intramolecular radical addition to indoles and pyrroles, Org. Lett. 12 (2010) 368–371.

[3] T. Maji, A. Karmakar, O. Reiser, Visible-light photoredox catalysis: dehalogenation of vicinal dibromo-, alpha-halo-, and alpha,alpha-dibromocarbonyl compounds, J. Org. Chem. 76 (2011) 736–739.

[4] J.M. Narayanam, C.R. Stephenson, Visible light photoredox catalysis: applications in organic synthesis, Chem. Soc. Rev. 40 (2011) 102–113.

[5] J. Xuan, W.J. Xiao, Visible-light photoredox catalysis, Angew. Chem. Int. Ed. 51 (2012) 6828–6838.

[6] Y. Shiraishi, T. Hirai, Selective organic transformations on titanium oxide-based photocatalysts, J. Photochem. Photobiol. C 9 (2008) 157–170.

[7] L. Ping, T. Teranishi, K. Asakura, M. Miyake, N. Toshima, Polymer-protected Ni/Pd bimetallic nano-clusters: preparation, characterization and catalysis for hydrogenation of nitrobenzene, J. Phys. Chem. B 103 (1999) 9673–9682.

[8] F.M. Dunnivant, R.P. Schwarzenbach, D.L. Macalady, Reduction of substituted nitrobenzenes in aqueous solutions containing natural organic matter, Environ. Sci. Technol. 26 (1992) 2133–2141.

[9] C. Avelino, S. Pedro, Chemoselective hydrogenation of nitro compounds with supported gold catalysts, Science 313 (2006) 332–334.

[10] F. Cárdenas-Lizana, S. Gómez-Quero, M.A. Keane, Exclusive production of chloroaniline from chloronitrobenzene over Au/TiO2 and Au/Al2O3, ChemSusChem 1 (2008) 215–221.

[11] M. Turáková, M. Králik, P. Lehocký, Ľ. Pikna, M. Smrčová, D. Remeteiová, A. Hudák, Influence of preparation method and palladium content on Pd/C catalysts activity in the liquid phase hydrogenation of nitrobenzene to aniline, Appl. Catal. A Gen. 476 (2014) 103–112.

[12] M. Liu, X. Zhu, R. Chen, Q. Liao, H. Feng, L. Li, Catalytic membrane microreactor with Pd/γ-Al2O3 coated PDMS film modified by dopamine for hydrogenation of nitrobenzene, Chem. Eng. J. 301 (2016) 35–41.

[13] P. Chen, A. Khetan, F. Yang, V. Migunov, P. Weide, S.P. Stürmer, P. Guo, K. Kähler, W. Xia, J. Mayer, H. Pitsch, U. Simon, M. Muhler, Experimental and theoretical understanding of nitrogen-doping-induced strong metal–support interactions in Pd/TiO2 catalysts for nitrobenzene hydrogenation, ACS Catal. 7 (2017) 1197–1206.

[14] S. Iihama, S. Furukawa, T. Komatsu, Efficient catalytic system for chemoselective hydrogenation of halonitrobenzene to haloaniline using PtZn intermetallic compound, ACS Catal. 6 (2015) 742–746.

[15] E. Boymans, S. Boland, P.T. Witte, C. Müller, D. Vogt, Chemoselective hydrogenation of functionalized nitroarenes using supported Mo promoted Pt nanoparticles, ChemCatChem 5 (2013) 431–434.

[16] D. Xu, Z. Hu, W. Li, S. Luo, Z. Xu, Hydrogenation in ionic liquids: an alternative methodology toward highly selective catalysis of halonitrobenzenes to corresponding haloanilines, J. Mol. Catal. A Chem. 235 (2005) 137–142.

[17] J. Zhao, C. Chen, B. Zhang, Z. Jiao, J. Zhang, J. Yang, Y. Qin, Tuning the selectivity of Pt-catalyzed tandem hydrogenation of nitro compounds via controllable NiO decoration by atomic layer deposition, Catal. Commun. 121 (2019) 48–52.

[18] C. Hao, X. Guo, M. Sankar, H. Yang, B. Ma, Y. Zhang, X. Tong, G. Jin, X. Guo, Synergistic effect of segregated Pd and Au nanoparticles on semiconducting SiC for efficient photocatalytic hydrogenation of nitroarenes, ACS Appl. Mater. Interfaces 10 (2018) 23029–23036.

[19] B. Lakshminarayana, G. Satyanarayana, C. Subrahmanyam, Bimetallic Pd–Au/TiO2 nanoparticles: an efficient and sustainable heterogeneous catalyst for rapid catalytic hydrogen transfer reduction of nitroarenes, ACS Omega 3 (2018) 13065–13072.

[20] X. Wang, F. Cárdenas-Lizana, M.A. Keane, Toward sustainable chemoselective nitroarene hydrogenation using supported gold as catalyst, ACS Sustain. Chem. Eng. 2 (2014) 2781–2789.

[21] A. Corma, C. González-Arellano, M. Iglesias, F. Sánchez, Gold complexes as catalysts: chemoselective hydrogenation of nitroarenes, Appl. Catal. A Gen. 356 (2009) 99–102.

[22] A. Corma, P. Concepcion, P. Serna, A different reaction pathway for the reduction of aromatic nitro compounds on gold catalysts, Angew. Chem. Int. Ed. 46 (2007) 7266–7269.

[23] T. Kamegawa, H. Seto, S. Matsuura, H. Yamashita, Preparation of hydroxynaphthalene-modified TiO2 via formation of surface complexes and their applications in the photocatalytic reduction of nitrobenzene under visible-light irradiation, ACS Appl. Mater. Interfaces 4 (2012) 6635–6639.

[24] B. Qiu, Y. Deng, Q. Li, B. Shen, M. Xing, J. Zhang, Rational design of a unique ternary structure for highly photocatalytic nitrobenzene reduction, J. Phys. Chem. C 120 (2016) 12125–12131.

[25] Z. Yan, Q. Chen, P. Xia, W. Ma, B. Ren, Strong interactions between Au nanoparticles and TiO2 mesocrystal: highly selective photocatalytic reduction of nitroarenes, Nanotechnology 27 (2016) 035707.

[26] A. Tanaka, Y. Nishino, S. Sakaguchi, T. Yoshikawa, K. Imamura, K. Hashimoto, H. Kominami, Functionalization of a plasmonic Au/TiO2 photocatalyst with an Ag co-catalyst for quantitative reduction of nitrobenzene to aniline in 2-propanol suspensions under irradiation of visible light, Chem. Commun. 49 (2013) 2551–2553.

[27] E.K. Piggott, T.O. Hope, B.W. Crabbe, P.M. Jalbert, G. Orlova, G.L. Hallett-Tapley, Exploiting the photocatalytic activity of gold nanoparticle-functionalized niobium oxide perovskites in nitroarene reductions, Catal. Sci. Technol. 7 (2017) 5758–5765.

[28] X. Liu, Y. Su, J. Lang, Z. Chai, X. Wang, A novel Au-loaded Na2Ta2O6 multifunctional catalyst: thermocatalytic and photocatalytic elimination of the poisonous nitrobenzene derivatives from wastewater under natural condition, J. Alloys. Compd. 695 (2017) 60–69.

[29] L. Fu, W. Cai, A. Wang, Y. Zheng, Photocatalytic hydrogenation of nitrobenzene to aniline over tungsten oxide-silver nanowires, Mater. Lett. 142 (2015) 201–203.

[30] R.M. Mohamed, F.M. Ibrahim, Visible light photocatalytic reduction of nitrobenzene using Ag/Bi2MoO6 nanocomposite, J. Ind. Eng. Chem. 22 (2015) 28–33.

[31] W. Han, L. Chen, W. Song, S. Wang, X. Fan, Y. Li, F. Zhang, G. Zhang, W. Peng, Synthesis of nitrogen and sulfur co-doped reduced graphene oxide as efficient metal-free cocatalyst for the photo-activity enhancement of CdS, Appl. Catal. B Environ. 236 (2018) 212–221.

[32] Y. Xu, Y. Chen, W.F. Fu, In Situ Preparation of CoP@CdS and its catalytic activity toward controlling nitro reduction under visible-light irradiation, ACS Omega 3 (2018) 1904–1911.

[33] L. Zhang, T. Xu, X. Zhao, Y. Zhu, Controllable synthesis of Bi2MoO6 and effect of morphology and variation in local structure on photocatalytic activities, Appl. Catal. B Environ. 98 (2010) 138–146.

[34] M. Wu, Y. Wang, Y. Xu, J. Ming, M. Zhou, R. Xu, Q. Fu, Y. Lei, Self-supported

Bi$_2$MoO$_6$ nanowall for photoelectrochemical water splitting, ACS Appl. Mater. Interfaces 9 (2017) 23647–23653.

[35] W. Dai, J. Yu, H. Xu, X. Hu, X. Luo, L. Yang, X. Tu, Synthesis of hierarchical flower-like Bi$_2$MoO$_6$ microspheres as efficient photocatalyst for photoreduction of CO$_2$ into solar fuels under visible light, CrystEngComm 18 (2016) 3472–3480.

[36] B. Zhang, J. Li, Y. Gao, R. Chong, Z. Wang, L. Guo, X. Zhang, C. Li, To boost photocatalytic activity in selective oxidation of alcohols on ultrathin Bi$_2$MoO$_6$ nanoplates with Pt nanoparticles as cocatalyst, J. Catal. 345 (2017) 96–103.

[37] M. Long, W. Cai, H. Kisch, Photoelectrochemical properties of nanocrystalline Aurivillius phase Bi$_2$MoO$_6$ film under visible light irradiation, Chem. Phys. Lett. 461 (2008) 102–105.

[38] W. Yang, X. Zhang, Y. Xie, Advances and challenges in chemistry of two-dimensional nanosheets, Nano Today 11 (2016) 793–816.

[39] J. Di, C. Yan, A.D. Handoko, Z.W. Seh, H. Li, Z. Liu, Ultrathin two-dimensional materials for photo- and electrocatalytic hydrogen evolution, Mater. Today 21 (2018) 749–770.

[40] M. Chhowalla, H.S. Shin, G. Eda, L.J. Li, K.P. Loh, H. Zhang, The chemistry of two-dimensional layered transition metal dichalcogenide nanosheets, Nat. Chem. 5 (2013) 263–275.

[41] G. Xiang, T. Li, J. Zhuang, X. Wang, Large-scale synthesis of metastable TiO$_2$(B) nanosheets with atomic thickness and their photocatalytic properties, Chem. Commun. 46 (2010) 6801–6803.

[42] K. Jing, J. Xiong, N. Qin, Y. Song, L. Li, Y. Yu, S. Liang, L. Wu, Development and photocatalytic mechanism of monolayer Bi$_2$MoO$_6$ nanosheets for the selective oxidation of benzylic alcohols, Chem. Commun. 53 (2017) 8604–8607.

[43] C. Lee, H. Yan, L.E. Brus, T.F. Heinz, J. Hone, S. Ryu, Anomalous lattice vibrations of single- and few-layer MoS$_2$, ACS Nano 4 (2010) 2695–2700.

[44] Q. Bao, Z. Han, W. Yu, Z. Ni, Y. Yan, Z.X. Shen, K.P. Loh, Y.T. Ding, Atomic-layer graphene as a saturable absorber for ultrafast pulsed lasers, Adv. Funct. Mater. 19 (2010) 3077–3083.

[45] X. Zhang, J. Zhang, J. Zhao, B. Pan, M. Kong, J. Chen, Y. Xie, Half-metallic

ferromagnetism in synthetic Co$_9$Se$_8$ nanosheets with atomic thickness, J. Am. Chem. Soc. 134 (2012) 11908–11911.

[46] H. Li, C. Liu, K. Li, H. Wang, Preparation, characterization and photocatalytic properties of nanoplate Bi$_2$MoO$_6$ catalysts, J. Mater. Sci. 43 (2008) 7026–7034.

[47] J. Bi, L. Wu, J. Li, Z. Li, X. Wang, X. Fu, Simple solvothermal routes to synthesize nanocrystalline Bi$_2$MoO$_6$ photocatalysts with different morphologies, Acta Mater. 55 (2007) 4699–4705.

[48] A. Martínez-de la Cruz, S. Obregón Alfaro, E. López Cuéllar, U. Ortiz Méndez, Photocatalytic properties of Bi$_2$MoO$_6$ nanoparticles prepared by an amorphous complex precursor, Catal. Today 129 (2007) 194–199.

[49] G. Tian, Y. Chen, W. Zhou, K. Pan, Y. Dong, C. Tian, H. Fu, Facile solvothermal synthesis of hierarchical flower-like Bi$_2$MoO$_6$ hollow spheres as high performance visible-light driven photocatalysts, J. Mater. Chem. 21 (2011) 887–892.

[50] Y. Zhou, Y. Zhang, M. Lin, J. Long, Z. Zhang, H. Lin, J.C. Wu, X. Wang, Monolayered Bi$_2$WO$_6$ nanosheets mimicking heterojunction interface with open surfaces for photocatalysis, Nat. Commun. 6 (2015) 8340.

[51] H. Li, J. Shang, Z. Ai, L. Zhang, Efficient visible light nitrogen fixation with BiOBr nanosheets of oxygen vacancies on the exposed {001} facets, J. Am. Chem. Soc. 137 (2015) 6393–6399.

[52] M. Guan, C. Xiao, J. Zhang, S. Fan, R. An, Q. Cheng, J. Xie, M. Zhou, B. Ye, Y. Xie, Vacancy associates promoting solar-driven photocatalytic activity of ultrathin bismuth oxychloride nanosheets, J. Am. Chem. Soc. 135 (2013) 10411–10417.

[53] S.C. Jensen, S. Bettis Homan, E.A. Weiss, Photocatalytic conversion of nitrobenzene to aniline through sequential proton-coupled one-electron transfers from a cadmium sulfide quantum Dot, J. Am. Chem. Soc. 138 (2016) 1591–1600.

[54] G. Chen, C. Xu, X. Huang, J. Ye, L. Gu, G. Li, Z. Tang, B. Wu, H. Yang, Z. Zhao, Z. Zhou, G. Fu, N. Zheng, Interfacial electronic effects control the reaction selectivity of platinum catalysts, Nat. Mater. 15 (2016) 564.

[55] Y. Shimodaira, H. Kato, H. Kobayashi, A. Kudo, Photophysical properties and photocatalytic activities of bismuth molybdates under visible light irradiation, J. Phys. Chem. B 110 (2006) 17790–17797.